PCCP

ROYAL SOCIETY OF CHEMISTRY

PAPER

View Article Online
View Journal | View Issue

Cite this: *Phys. Chem. Chem. Phys.*, 2023, **25**, 17352

Temperature-resolved nanoscale hydration of a layered manganese oxide†

N. Tan Luong, Hanna Oderstad, Michael Holmboe and Jean-François Boily *

Received 17th March 2023,
Accepted 22nd May 2023

DOI: 10.1039/d3cp01209c

rsc.li/pccp

Water films captured in the interlayer region of birnessite (MnO_2) nanosheets can play important roles in biogeochemical cycling, catalysis, energy storage, and even atmospheric water harvesting. Understanding the temperature-dependent loadings and properties of these interlayer films is crucial to comprehend birnessite reactivity when exposed to moist air and temperature gradients. Using vibrational spectroscopy we show that birnessite intercalates one water (1W) monolayer at up to ~40 °C, but that loadings decrease by half at up to 85 °C. Our results also show that the vibrational properties of intercalated water are unaffected by temperature, implying that the hydrogen bonding network of water remains intact. Using molecular simulations, we found that the lowered water storage capacity at high temperatures cannot be explained by variations in hydrogen bond numbers or in the solvation environments of interlayer K^+ ions initially present in the interlayer region. It can instead be explained by the compounded effects of larger evolved heat, as inferred from immersion energies, and by the larger temperature-driven mobility of water over that of K^+ ions, which are electrostatically bound to birnessite basal oxygens. By shedding new light on the temperature-driven intercalation of water in a nanolayered mineral, this study can guide future efforts to understand the (geo)chemical reactivity of related materials in natural and technological settings.

Introduction

Birnessite (MnO_2) is a highly reactive layered manganese oxide widely distributed in terrestrial soils and sediments, as well as in the form of ferromanganese deposits in the deep ocean.[1] The structure of this phyllomanganate mineral consists of stacked edge-sharing MnO_6 sheets (Fig. 1) with a charge imbalance resulting from various Mn oxidation states (Mn^{IV}, Mn^{III}, and Mn^{II}), as well as the presence of cationic vacancies.[1–3] The charge imbalance is compensated by countercations (*e.g.*, H^+, Na^+, K^+, Mg^{2+} and Ca^{2+}) intercalated into the interlayer region. This region also has the ability to host nanometrically thick water films with distinct properties from those of liquid water.[4]

Intercalated films greatly control birnessite stability[5,6] and water-driven processes, including electron transfer and ion exchange. Works on molecular orientations,[7] cation–water interactions,[5,6,8] thermal stability,[5,6,9] and populations[4] of this internal hydration environment advanced the knowledge needed for understanding reactions of importance to nature and technology. Examples of these applications include mass transport reactivity in (bio)geochemistry,[10–14] water desalination[15]

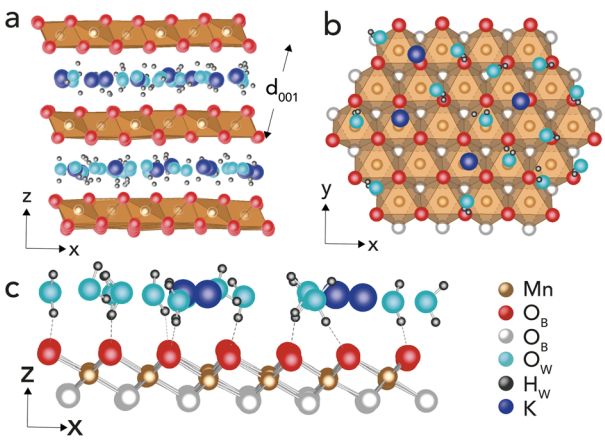

Fig. 1 Schematic representations of K^+-birnessite with one intercalated layer (1W: 1.33 H_2O per unit cell). (a) Side/edge view showing that hydration waters (O_W turquoise; H_W black) for potassium ions (K; dark blue) lie in a single plane. The interlayer d_{001} spacing in relation to the crystal structure is also shown. (b) Basal plane view showing spatial distributions of hydration waters and potassium over the basal plane oxygens (O_B; red on top and white at the bottom side of the MnO_2 nanosheet). (c) Side/edge view showing hydrogen bonds established between hydration waters (donors) and basal plane oxygens (O_B). These images were generated using a snapshot of molecular dynamics simulations from this work and then edited for illustration purposes.

Department of Chemistry, Umeå University, Umeå SE-901 87, Sweden.
E-mail: jean-francois.boily@umu.se

† Electronic supplementary information (ESI) available. See DOI: https://doi.org/10.1039/d3cp01209c

and purification,[16] removal of air-bone organic contaminants,[17,18] catalysis,[19] water oxidation,[20] batteries,[21,22] nuclear waste management,[23] and atmospheric water harvesting.[24]

Birnessite formed in aqueous solutions usually intercalate one (1W; 7 Å birnessite) to two (2W; 10 Å birnessite, or buserite) water monolayers.[4] Interlayer ordering is typically controlled by MnO_6 basal sheet crystallinity.[25] At high levels of crystallinity, water molecules have minimal water–water interactions and establish only one hydrogen bond with O_B sites exposed on MnO_6 basal sheets (Fig. 1). They also serve as the first hydration shell to intercalate cations (*e.g.* K^+ in K^+-birnessite).[4,6,7] Interlayer identity can, at the same time, influence the thermal stability of the hydration layer. For example, monovalent cations promote dehydration at lower temperatures than divalent cations.[6] Removing water from the interlayer promotes, in turn, structural disordered birnessite at a temperature of 200 °C in Li^+-birnessite or even a cryptomelane-like (KMn_8O_{16}) structure in K^+-birnessite at 400–600 °C.[5] Birnessite that underwent dehydration, yet that retained its crystallographic structure, can only be rehydrated up to a single monolayer (1W = 1.33 H_2O per unit cell) when exposed to moist air under ambient conditions.[4] Previous studies[4–6,25,26] revealed the structure, stability and reactivity of intercalated water films. However, some studies were conducted under extreme conditions of temperature and pressure,[5,6] which may have a compromised birnessite structure.

This study focuses on investigating the thermal behaviours of intercalated water in birnessite,[4,27] and is built upon a previous study by our group on these reactions at 25 °C.[4] In this work, we focused on K^+-birnessite because it dehydrates at low temperature while its structure remains unchanged at temperatures as high as 400 °C.[5,6] We used vibrational spectroscopy to monitor the ability of K^+-birnessite to trap and release water vapour across a range of temperatures. Molecular simulations provided new insights into the temperature-resolved properties of intercalated water. As temperature is a critical factor in controlling the reaction kinetics, this work serves as a basis for further studies on the behaviour of birnessite in hot and moist air.

Methodology

Experimental

Synthesis and characterization. K^+-birnessite was synthesised by the reduction of $KMnO_4$ under acidic conditions.[11,28] A vigorously stirred 2.5 L solution of 0.4 M $KMnO_4$ kept at 90 °C was titrated with a 166 mL solution of 12 M HCl.[11] The suspension was continuously stirred and kept at 90 °C for an additional 10 min after the titration. The resulting "acid birnessite"[11] suspension was then washed with MilliQ water by repeated cycles of centrifugation/decantation until the conductivity was ~10 μS cm^{-1}. The washed materials were then stored as the aqueous suspension in polyethylene bottles at 4 °C for a 3-year period prior to the onset of this work.

A portion of the sample was oven-dried at 60 °C for particle characterization, and a detailed account of which was already presented in our previous study.[4] Briefly, the solid phase was a low crystalline birnessite phase with a Brunauer–Emmett–Teller (B.E.T.)[29] specific surface area of 59.2 m^2 g^{-1}. From X-ray photoelectron spectroscopy (XPS), the particles had a surface Mn : O : K composition of 1.00 : 1.49 : 0.20. We note that the O/Mn ratio was lower than the expected stoichiometric value of 2 because XPS probes the topmost 10 nm region of the samples, and because of the loss of chemisorbed water under ultra-vacuum conditions. XPS also revealed that the surface of birnessite had a Mn atomic oxidation state (AOS) of 3.69. Using the method of Ilton *et al.*[30] this AOS arises from a mixture of 72% Mn^{IV}, 25% Mn^{III}, and 3% Mn^{II}.

Water vapour intercalation experiments

Binding of water vapour on birnessite during dynamic vapour sorption (DVS)[31] was monitored by Fourier transform infrared (FTIR) spectroscopy. All FTIR spectra were collected using a Bruker Vertex 70/V FTIR spectrometer, equipped with a DLaTGS detector. The spectra were collected at a resolution of 4.0 cm^{-1} in the 600–4000 cm^{-1} range, and at a forward/reverse scanning rate of 10 kHz. Each spectrum was an average of 500 scans, taking a total of 7.14 min per spectrum. A representative spectrum of dry birnessite is shown in Fig. S1 (ESI†).

Centrifuged wet pastes of birnessite were deposited on the diamond window of an attenuated total reflectance (ATR) cell (Golden Gate N29328 by Specac). This ATR cell was equipped with a heating unit enabling measurements at a temperature of 80 °C. The wet birnessite film was then covered with a modified Golden Gate cryo-chamber equipped with a gas inlet and an outlet, enabling a flow of 500 mL min^{-1} N_2(g) over the sample. Prior to each experiment, wet pastes were first dried and then equilibrated under a steam dry N_2(g) at pre-selected temperatures in the range of 30–80 °C (30, 40, 50, 60, 70, and 80 °C). FTIR spectra were thereafter collected to monitor the loss of water using the absorbances of the O–H stretching and bending bands of water.

Water vapour adsorption/desorption isotherms were then collected at each temperature by exposing birnessite to a 500 mL min^{-1} flow of 10 pre-selected partial pressures of H_2O in the range of 0–3.11 kPa (*i.e.* 0.4–95% relative humidity at 25 °C) with 98.2–101.3 kPa N_2 (g). A 1 h equilibration period was allowed between each change in H_2O content. These gases were prepared at 25 °C by mixing pre-determined proportions of humid N_2 (g) produced from a humidity generator module (proUmid MHG32) with dry N_2 (g). Water vapour pressures were continuously monitored using both a sensor equipped with the module and a nondispersive InfraRed device (LI-7000, Licor Inc).

To study the temperature-resolved changes in the birnessite-bound water, we analysed the O–H stretching and bending vibrational regions by spectral deconvolution. Following preliminary efforts testing various distribution functions, we found that absorbances of the O–H stretching region (A_{O-H}) were best modelled by a linear combination of Gaussian components:

$$A_{O-H} = \sum_{1}^{n} A_{n,O-H,\,max} e^{-((\nu-\nu_n)/\sigma_n)^2} \quad (1)$$

Here, $A_{n,O-H,max}$ is the maximal absorbance of the nth component centred at wavenumber ν_n, and with the width of the distribution σ_n. Absorbances of the water bending region (A_{H-O-H}) were, in turn, best described by a linear combination of Lorentzian components:

$$A_{H-O-H} = \sum_{1}^{n} \frac{A_{n,H-O-H,\,max}}{1 + ((\nu - \nu_n)/\sigma_n)^2}. \quad (2)$$

Here, $A_{n,H-O-H,max}$ is also the maximal absorbance of the nth component centred at wavenumber ν_n, and with the width of the distribution σ_n. All spectra were normalised for the Mn–O stretching band (600 cm^{-1}; Fig. S1, ESI†) to account for variations in sample quantity. The background was corrected using a linear function prior to peak-fitting. All calculations were performed in Matlab R2022a (The Mathworks, Inc.).

Temperature programmed desorption. The relative thermal stability of intercalated water was resolved by temperature programmed desorption (TPD). Experiments were performed on birnessite first by drying under N_2 (g) followed by exposing to a flow of 500 mL min^{-1} of 3.11 kPa H_2O for 1 h at 25 °C. The samples were reacted in an optical transmission cell (AABSPEC-#2000-A) for vibrational spectroscopy and then exposed to vacuum of less than 0.3 kPa. These samples were then exposed to a heating gradient of 10 °C min^{-1} from 40 to 400 °C, during which time the FTIR spectra were collected as H_2O was released from the interlayer region of birnessite.

Molecular simulations

Molecular dynamics (MD) simulations of K^+-saturated birnessite were carried out to resolve the structure and dynamics of hydration in the interlayer region. This was achieved by successive simulations at 10 selected temperatures (0, 5, 15, 25, 35, 45, 55, 65, 75, and 85 °C) of birnessite supercells intercalated with decreasing amounts of water. The supercells consisted of $6 \times 12 \times 4$ unit cells (UCs)[7] having an initial composition of $K_{144}[Mn_{576}O_{1152}] \times (H_2O)_{3840}$, hence 0.25 K^+/UC and an initial water content of 13.333 H_2O/UC. After equilibration by energy minimisation followed by 2 ns of volume and pressure optimization, 61 successive productions were run in the isobaric-isothermal (*NPT*) ensemble. All simulations were carried out at a 1 fs time step. In between each of the production runs, 16 water molecules (corresponding to approx. 0.22 H_2O/UC) of randomly selected water molecules were removed from each interlayer region, all while preserving the same d_{001}. Each water removal step was followed by a 500 ps pre-equilibration run, which was not included in the analysis.

All simulations were carried out using GROMACS,[32] using a 1.0 nm cutoff for the direct van der Waals and Coulombic interactions. Long-range Coulombic interactions were treated using the particle-mesh Ewald (PME) method. The birnessite lattice was, just as in our recent study,[4] modelled with $Mn^{3.75+}$ as in the study of Cygan *et al.*.[33] However, using the recently reported Lennard–Jones forcefield parameters of Newton and Kwon,[34] water was simulated using the SPC/E model,[35] and K^+ ions were simulated with SPC/E compatible ion-pair potentials from the study of Joung and Cheatham.[36]

Simulation results were thereafter analysed for d_{001}, hydrogen bonding, K^+–O coordination, and K^+ and water diffusion coefficients. Diffusion coefficients were calculated with the Gromacs utility gmx msd from 3 ns production runs over individual 250 ps segments, omitting the first 50 ps in each. Comparison of diffusion coefficients obtained in the canonical (*NVT*) ensemble confirmed that the short simulations and large box sizes did not introduce deviations in values that could otherwise be expected[37] from the simulation run in the *NPT* ensemble (Fig. S2, ESI†).

Finally, energetics of stable hydration states were determined using the following equation:[38,39]

$$Q(N) = U(N) - U(N^\circ) - U_{bulk}(N - N^\circ) \quad (3)$$

where $Q(N)$ is the hydration immersion energy (J g^{-1}) relative to a reference hydration state N°, N is H_2O/UC, $\langle U \rangle$ is the time-averaged potential energy, and U_{bulk} is the mean interaction energy of a bulk SPC/E water molecule, at each temperature. In practice, U_{bulk} is a fitting parameter making $Q(N)$ reaching a similar value to the bulk vaporisation energy of water at high N.

Results and discussion

Spectral response of temperature-resolved water intercalation

FTIR spectra provided direct insight into water bound to the K^+-birnessite bulk and surfaces up to 80 °C (Fig. 2; the full data set is shown in Fig. S3, ESI†). These were given by the O–H stretching (ν_1; *e.g.* Fig. 2a and b) and the bending (ν_2; *e.g.* Fig. 2c and d) vibrational regions of water. The absorbances of these regions responded directly to variations in water vapour content (0.01–3.11 kPa H_2O) during both adsorption and desorption legs.

Vapour pressure- and temperature-dependent water loadings were more clearly captured using the integrated normalised absorbances of both O–H stretching (Fig. 2e) and water bending (Fig. 2f) regions. First, the shape of these spectroscopically derived adsorption isotherms was consistent with our previous[4] microgravimetric data (Fig. 2g). Both revealed a type II adsorption/desorption[40] isotherm, with comparable hysteresis in the desorption leg. Our previous modelling efforts[4] expressed water uptake chiefly in terms of intercalated water, reaching a maximum coverage of a single water monolayer (1W) at a high humidity (~1.33 H_2O per unit cell (UC)). Adsorbed and condensed water accounted for a smaller fraction of water, with the latter accounting for the larger loadings at high humidity only. From the absorbances of the vibrational spectra, we also found that water loadings were lowered by ~50% at temperatures exceeding ~40 °C (Fig. 2e and f). These temperature-adjusted isotherms also showed that even atmospherically relevant partial pressures of water (*e.g.* up to 3.11 kPa H_2O) at high temperatures could not saturate the interlayer region of birnessite with water.

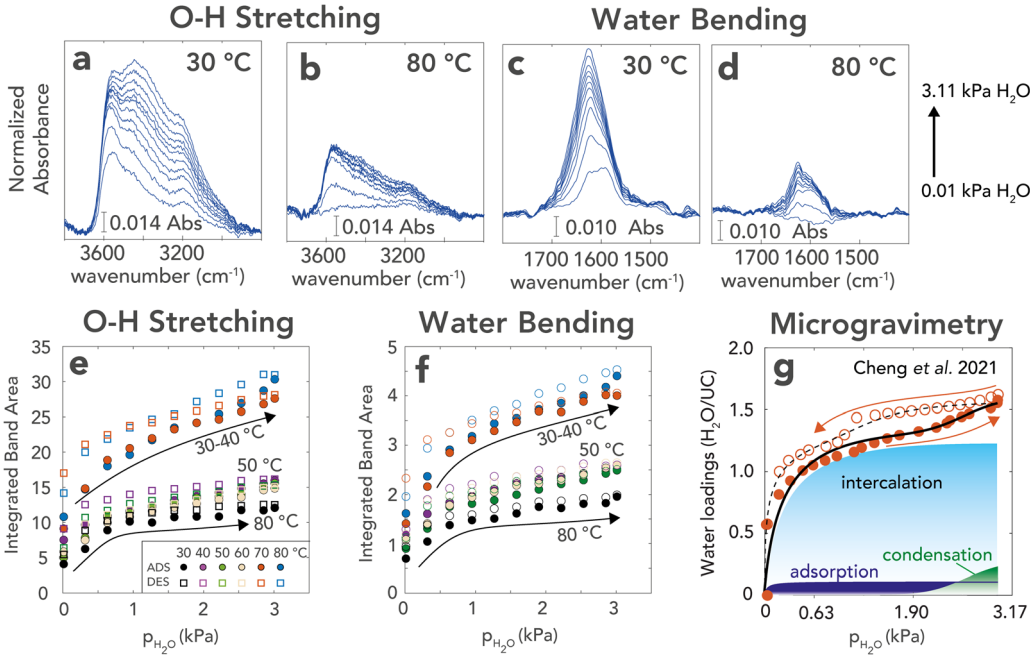

Fig. 2 (a)–(d) FTIR spectra of birnessite exposed to a 500 mL min^{-1} flow of 0–3.11 kPa H_2O in N_2(g) (a total pressure of 101 kPa) during the adsorption leg. See Fig. S3 (ESI†) for the complete data set for both adsorption and desorption legs at all temperatures. All absorbances were normalised for the quantity of MnO_2 based on the absorbance of the Mn–O stretching band at 600 cm^{-1} (Fig. S1, ESI†). (e) and (f) Integrated band areas of all normalised spectra of Fig. S3 (ESI†) (ADS = adsorption; DES = desorption) in the (e) O–H stretching and (f) water bending regions. (g) Microgravimetric and model predictions from our previous work[4] showing the relative concentrations of intercalated, adsorbed and condensed water at 25 °C.

Saturation at temperatures exceeding 40 °C can, as such, only be achieved in pressurised environments or in liquid water.

To deepen our understanding of the humidity dependence of intercalated water, the O–H stretching (ν_1) and water bending (ν_2) regions were resolved by spectral deconvolution (Fig. 3 and 4, and Fig. S4, ESI†). The O–H stretching region was modelled at all temperatures in terms of (Gaussian-shaped; eqn (1)) bands at (i) 3574 ± 15 cm^{-1} from free (isolated) O–H bonds of water bonded to basal oxygens (O_B; Fig. 1) of the interlayer region, (ii) 3470 ± 9 cm^{-1} from hydrogen-bonded water (weak intermolecular coupling[41,42]), (iii) 3276 ± 30 cm^{-1} from hydrogen-bonded water (strong intermolecular coupling[41,42]) and Fermi resonance ($2\,\nu_2$) of the water bending mode (ν_2 = 1622 cm^{-1}), and (iv) 3189 ± 2 cm^{-1} likely representing a distinct sub-population of intercalated hydrogen-bonded water molecules. Band positions were not greatly affected by temperature (Fig. S4, ESI†).

These assignments were supported by the following water vapour pressure dependence on component absorbances (Fig. 3g–l). O–H groups from intercalated water (3574 and 3189 cm^{-1}) followed a type II adsorption isotherm akin to our modelling of the microgravimetry data, plateauing at ~0.6 kPa H_2O (Fig. 2g). The number of hydrogen-bonded water molecules increased throughout the range of 0–3.11 kPa, first through a steep increase with humidity akin to that of intercalated water, and through a lower response to humidity from externally bound (adsorbed and condensed) water (Fig. 2g).

Modelling of the water bending region revealed (Lorentzian-shaped; eqn (2)) bands at (i) ~1592 ± 10 cm^{-1} from intercalated water and (ii) ~1622 ± 8 cm^{-1} from liquid-like water. Again, band positions were not systematically affected by temperature (Fig. S4, ESI†). The water vapour pressure dependence of the 1592 cm^{-1} band chiefly aligned with that of O–H stretching bands of intercalated water (3574 and 3189 cm^{-1}). The lower bending frequencies of the intercalated water also aligned with the expectation of a strong hydrogen bond with the basal oxygen sites of the interlayer region of birnessite. The ~1622 cm^{-1} term, on the other hand, continued to increase in absorbance as a result of the increased water loadings. This can be taken as evidence that liquid water-like films appeared at birnessite nanoparticle surfaces.

Finally, the temperature-dependence of component absorbances (Fig. 4) reflected the exothermic nature of the water binding reactions, as expected from calorimetric studies.[43] Total absorbances suggest a loss of water of at least ~40% when birnessite was heated from 30 °C up to at least 50 °C. This loss in absorbance can be explained by the removal of all types of water from birnessite (Fig. 4b and c). In particular, the loss of bands from water molecules that were hydrogen-bonded to basal oxygens (3574, 3189 and 1592 cm^{-1}) suggested that interlayer water films were preferentially removed within the 40–50 °C range.

The temperature dependence of the band components (Fig. 4b) also revealed no preferential loss in water molecules that were hydrogen-bonded to basal oxygens (3574 and 3189 cm^{-1}) over those that were more weakly hydrogen-bonded to water (3470 cm^{-1}). The loss of the 3276 cm^{-1} band (Fig. 4b) however indicated that water–water interactions were preferentially disrupted with temperature.[44] This can also be seen in the water

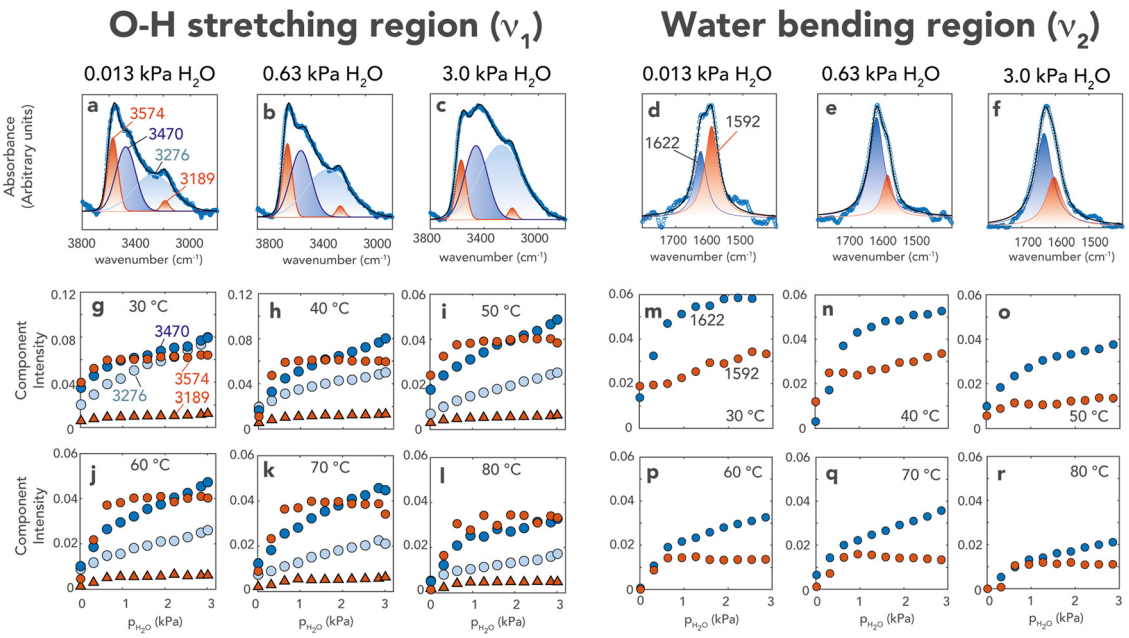

Fig. 3 Band deconvolution of the O–H stretching (a)–(c) and water bending (d)–(f) regions for samples reacted at 30 °C. Examples of fitting are shown for three water partial pressures only. (g)–(l) Gaussian component absorbances ($A_{n,O\text{-}H,max}$ in eqn (1)) for the O–H stretching region and (m)–(r) Lorentzian component absorbances ($A_{n,O\text{-}H,max}$ in eqn (2)) are shown for all temperatures over the range of 0–3.11 kPa H_2O. Corresponding component wavenumbers (ν_n in eqn (1) and (2)) are shown in Fig. S4 (ESI†).

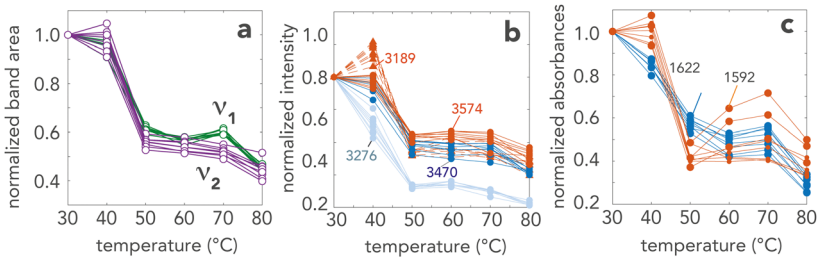

Fig. 4 Temperature dependence of water binding to birnessite, using the adsorption data from Fig. 2. (a) Numerically integrated band area of the O–H stretching (ν_1) and water bending (ν_2) regions. Absorbances of the (b) Gaussian band components ($A_{n,O\text{-}H,max}$ in eqn (1)) of the O–H stretching region and (c) Lorentzian band components ($A_{n,O\text{-}H,max}$ in eqn (2)) of the water bending region. Each value was normalised for the (a) band area or (b) and (c) component absorbance for respective values at each water partial pressure at 30 °C.

bending region by temperature-programmed desorption in Fig. S5 (ESI†).

Molecular structure and dynamics of water intercalation

To explore how temperature affects water structure and dynamics in the interlayer region of birnessite, MD simulations were performed at 10 preselected temperatures between 0 and 85 °C. These simulations build upon those we previously reported for intercalated water at 25 °C, and more than covered the experimental range considered in this study.

Simulations (Fig. 5–7 and Fig. S6, S7, ESI†) showed that the interlayer spacings for one (1W) and two water monolayers (2W) were practically independent of temperature (Fig. 5a). The 2W state, known as buserite, can however only be attained by submerging birnessite in liquid water.[1,45,46] Additionally, immersion energies in the 1W state were larger at higher temperatures, a result consistent with the concept for more exothermic reactions at high temperatures (Fig. 5b).[43]

In previous studies,[47,48] our 1W hydration state was nearly-monoclinic, with cell dimensions that were nearly independent of temperature (a = 0.511, b = 0.295, and c = 0.706 nm; d_{001} = 0.685 nm because UC β = 104.0°; Fig. 1). Additionally, K^+ and water oxygens (O_W) were consistently at the centre of the interlayer region between oxygens of the basal face (O_b) of birnessite, a result aligning with previous MD work.[33] Total K^+ coordination numbers (~9.7 O/K^+) were consistently from ~5.2 O_w on the same plane of the 1W water layer, and ~4.5 O_b from both the basal faces of MnO_2 per K^+ ion. These numbers were also independent of temperature for 1W.

The most relevant piece of information that links back to our FTIR results relates to hydrogen bond numbers, as these

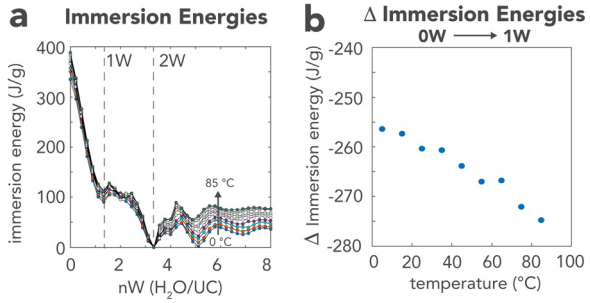

Fig. 5 (a) Predicted immersion energy profiles *versus* water loadings (H_2O/UC; UC = unit cell) showing the 1W state at 1.33 H_2O/UC (5.33 H_2O/K^+; d_{001}-spacing = 0.685 nm) and the 2W state at 3.33 H_2O/UC (13.33 H_2O/K^+; d_{001}-spacing = 1.00 nm). (b) Temperature dependence of immersion energy at 1W over the range of 0–85 °C. See Fig. S6 (ESI†) for immersion energies against d_{001}-spacing and Fig. S7 (ESI†) against water H_2O/UC for comparison.

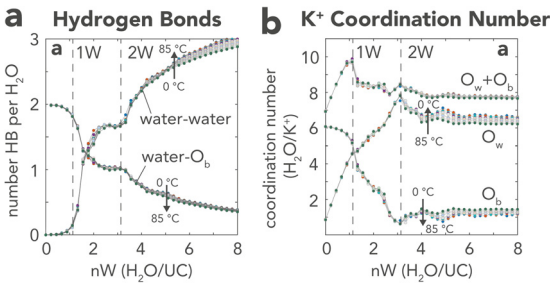

Fig. 6 MD-simulated basal spacing dependence (d_{001}) on (a) hydrogen bond numbers and (b) K^+ coordination numbers. The first-shell coordination of K^+ to oxygens belongs to either water (O_W) or birnessite (O_b) oxygens. Coordination numbers were calculated from the radial distribution functions up to the minima of the first coordination shell at 0.35 nm.

directly affect spectral shapes and positions. These were dominated by interactions with basal oxygens (1.83 O_b/H_2O) and a minute portion involved in water–water interactions (0.13 bond/H_2O). These results consequently align with our previous finding that the increase in vibrational bands of 'liquid water-like' components (1592, 3189 and 3574 cm^{-1} in Fig. 2 and 3) was not from intercalated water but adsorbed and condensed water at birnessite particle surfaces (Fig. 2g).

From these results, we conclude that variations in water loadings with temperature can only be explained in terms of the dynamics of the 1W layer, as the structure and molecular interactions remained unchanged (Fig. 6). This aligns with the large temperature-driven increases in water and K^+ diffusion coefficients (Fig. 7). While the 1W state had the lowest diffusion coefficients for any nW state (Fig. 7a), these values increased by nearly one order of magnitude at 85 °C (Fig. 7c). Those of K^+ remained, on the other hand, relatively unchanged with temperature. Because K^+ (0.266 nm) and H_2O (0.275 nm) have similar sizes, the chief factor influencing the smaller temperature-dependent diffusivity of K^+ is its charge. As such, while increasing temperatures effectively enhanced water mobility along the 1W layer, the K^+ ion mobility was systematically lower due to electrostatic interactions with O_b sites (4.5 O_b/K^+ in 1W). K^+ diffusivity in the 2W state, in contrast, increased on par with water with temperature because the first shell K^+–O_b interactions ($\ll$1 O_b/K^+) were replaced by K^+–O_w interactions (Fig. 6b). We therefore attribute the diminished capability of the interlayer region of birnessite to store water in the 1W state at high temperatures to the compounded effects of (i) increased evolved heat (*i.e.* exothermicity), and (ii) the larger mobility of water over that of K^+ with temperature.

Conclusions

Using vibrational spectroscopy and molecular modelling, we showed that birnessite intercalates one water (1W) monolayer at up to ~40 °C. Above this temperature, water loadings decreased ~2-fold as a result of the increased heat evolved, and the larger mobility of water compared to that of K^+ with temperature. While these factors destabilized water films at high temperatures, hydrogen bond numbers and K^+ solvation environments remained unchanged. The information gathered in this work consequently clarified the role of temperature on the interlayer hydration environment of birnessite. This information should be especially useful in the study of hot water-unsaturated natural environments (*e.g.* vadose zones of soils) as well as in several technological applications including energy storage and atmospheric water capture by these, and related, materials.

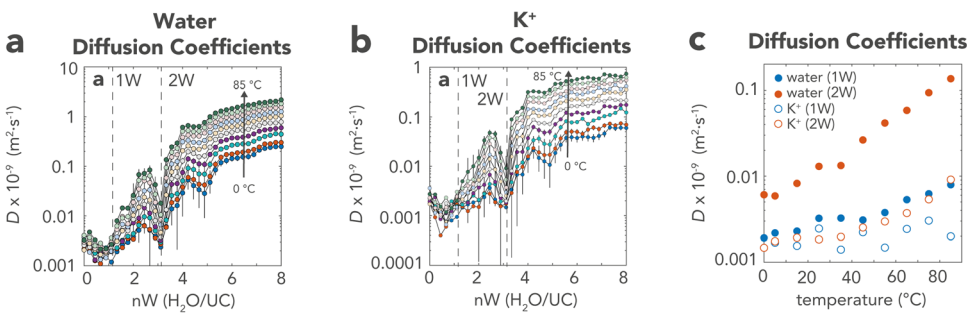

Fig. 7 MD-simulated diffusion coefficients of (a) water and (b) K^+ as a function of interlayer water numbers (nW). Dashed vertical lines indicate ideal 1W and 2W hydration states. (c) Temperature dependence of diffusion coefficients of water and K^+ as 1W and 2W. Note that the ordinate axis of Fig. 8c from the study of Cheng *et al.*,[4] also reporting water diffusion coefficients, should read as '$D \times 10^{-9}$' and not '$D \times 10^{-10}$'.

Author contributions

NTL and JFB conceived this study. TL and HO performed the experimental work. MB performed molecular dynamics simulations. JFB performed numerical analyses of vibrational spectra. All authors co-wrote this article.

Conflicts of interest

There are no conflicts to declare.

Acknowledgements

This work was supported by the Swedish Research Council (2020-04853) and Formas (2022-01246) to J. F. B. Molecular simulations were enabled by resources provided to J. F. B. and M. H. by the Swedish National Infrastructure for Computing (SNIC) at High Performance Computational Cluster North (HPC2N) partially funded by the Swedish Research Council through grant agreement no. 2018-05973.

References

1 J. E. Post, *Proc. Natl. Acad. Sci.*, 1999, **96**, 3447–3454.
2 V. A. Drits, E. Silvester, A. I. Gorshkov and A. Manceau, *Am. Mineral.*, 1997, **82**, 946–961.
3 B. Lanson, V. A. Drits, E. Silvester and A. Manceau, *Am. Mineral.*, 2000, **85**, 826–838.
4 W. Cheng, J. Lindholm, M. Holmboe, N. T. Luong, A. Shchukarev, E. S. Ilton, K. Hanna and J.-F. Boily, *Langmuir*, 2021, **37**, 666–674.
5 D. C. Golden, J. B. Dixon and C. C. Chen, *Clays Clay Miner.*, 1986, **34**, 511–520.
6 A. E. Johnson and E. J. Post, *Am. Mineral.*, 2006, **91**, 609–618.
7 J. E. Post, P. J. Heaney and Y. Cho, *Am. Mineral.*, 2011, **96**, 534–540.
8 S. Park and K. D. Kwon, *ACS Earth Space Chem.*, 2021, **5**, 3159–3169.
9 H. S. Choi, S. J. Kim and J. J. Kim, *Geosci. J.*, 2004, **8**, 273–279.
10 D. Banerjee and H. W. Nesbitt, *Geochim. Cosmochim. Acta*, 2001, **65**, 1703–1714.
11 M. Villalobos, B. Toner, J. Bargar and G. Sposito, *Geochim. Cosmochim. Acta*, 2003, **67**, 2649–2662.
12 M. Villalobos, I. N. Escobar-Quiroz and C. Salazar-Camacho, *Geochim. Cosmochim. Acta*, 2014, **125**, 564–581.
13 M. H. H. Fischel, J. S. Fischel, B. J. Lafferty and D. L. Sparks, *Geochem. Trans.*, 2015, **16**, 15.
14 Q. Wang, P. Yang and M. Zhu, *Geochim. Cosmochim. Acta*, 2019, **250**, 292–310.
15 Z. Y. Leong and H. Y. Yang, *ACS Appl. Mater. Interfaces*, 2019, **11**, 13176–13184.
16 W.-T. Jiang, P.-H. Chang, Y.-S. Wang, Y. Tsai, J.-S. Jean, Z. Li and K. Krukowski, *J. Hazard. Mater.*, 2013, **250–251**, 362–369.
17 Y. Liu, H. Zhou, R. Cao, X. Liu, P. Zhang, J. Zhan and L. Liu, *Appl. Catal., B*, 2019, **245**, 569–582.
18 J. Wang, P. Zhang, J. Li, C. Jiang, R. Yunus and J. Kim, *Environ. Sci. Technol.*, 2015, **49**, 12372–12379.
19 Q. Kang, L. Vernisse, R. C. Remsing, A. C. Thenuwara, S. L. Shumlas, I. G. McKendry, M. L. Klein, E. Borguet, M. J. Zdilla and D. R. Strongin, *J. Am. Chem. Soc.*, 2017, **139**, 1863–1870.
20 B. A. Pinaud, Z. Chen, D. N. Abram and T. F. Jaramillo, *J. Phys. Chem. C*, 2011, **115**, 11830–11838.
21 F. Gálvez, M. Cabello, P. Lavela, G. F. Ortiz and J. L. Tirado, *Molecules*, 2020, **25**, 924.
22 X. Shan, F. Guo, D. S. Charles, Z. Lebens-Higgins, S. Abdel Razek, J. Wu, W. Xu, W. Yang, K. L. Page, J. C. Neuefeind, M. Feygenson, L. F. J. Piper and X. Teng, *Nat. Commun.*, 2019, **10**, 4975.
23 S. Bevara, P. Giri, S. N. Achary, G. Bhallerao, R. K. Mishra, A. Kumar, C. P. Kaushik and A. K. Tyagi, *J. Environ. Chem. Eng.*, 2018, **6**, 7200–7213.
24 J. Wang, Y. Dang, A. G. Meguerdichian, S. Dissanayake, T. Kankanam-Kapuge, S. Bamonte, Z. M. Tobin, L. A. Achola and S. L. Suib, *Environ. Sci. Technol. Lett.*, 2020, **7**, 48–53.
25 R. M. Potter and G. R. Rossman, *Am. Mineral.*, 1979, **64**, 1199–1218.
26 N. Birkner, S. Nayeri, B. Pashaei, M. M. Najafpour, W. H. Casey and A. Navrotsky, *Proc. Natl. Acad. Sci. U. S. A.*, 2013, **110**, 8801–8806.
27 M. Yeşilbaş, M. Holmboe and J.-F. Boily, *ACS Earth Space Chem.*, 2018, **2**, 38–47.
28 R. M. McKenzie, *Mineral. Mag.*, 1971, **38**, 493–502.
29 S. Brunauer, P. H. Emmett and A. Teller, *J. Am. Chem. Soc.*, 1938, **60**, 309–319.
30 E. S. Ilton, J. E. Post, P. J. Heaney, F. T. Ling and S. N. Kerisit, *Appl. Surf. Sci.*, 2016, **366**, 475–485.
31 G. Zografi and M. J. Kontny, *Sorption of Water by Solids*, Marcel Dekker, New York, 1995.
32 M. J. Abraham, T. Murtola, R. Schulz, S. Páll, J. C. Smith, B. Hess and E. Lindahl, *SoftwareX*, 2015, **1–2**, 19–25.
33 R. T. Cygan, J. E. Post, P. J. Heaney and J. D. Kubicki, *Am. Mineral.*, 2012, **97**, 1505–1514.
34 A. G. Newton and K. D. Kwon, *Geochim. Cosmochim. Acta*, 2018, **235**, 208–223.
35 H. J. C. Berendsen, J. R. Grigera and T. P. Straatsma, *J. Phys. Chem.*, 1987, **91**, 6269–6271.
36 I. S. Joung and T. E. Cheatham, III, *J. Phys. Chem. B*, 2008, **112**, 9020–9041.
37 S. von Bülow, J. T. Bullerjahn and G. Hummer, *J. Chem. Phys.*, 2020, **153**, 021101.
38 D. E. Smith, *Langmuir*, 1998, **14**, 5959–5967.
39 M. Holmboe and I. C. Bourg, *J. Phys. Chem. C*, 2014, **118**, 1001–1013.
40 K. S. W. Sing, D. H. Everett, R. A. W. Haul, L. Moscou, R. A. Pierotti, J. Rouquerol and T. Siemieniewska, *Pure Appl. Chem.*, 1985, **57**, 603–619.
41 L. Shi, S. M. Gruenbaum and J. L. Skinner, *J. Phys. Chem. B*, 2012, **116**, 13821–13830.

42 J. Skinner, B. Auer and Y. Lin, *Advances in Chemical Physics*, 2010.
43 N. Birkner and A. Navrotsky, *Am. Mineral.*, 2012, **97**, 1291–1298.
44 Y. Maréchal, *J. Mol. Struct.*, 2011, **1004**, 146–155.
45 D. C. Golden, C. C. Chen and J. B. Dixon, *Clays Clay Miner.*, 1987, **35**, 271–280.
46 R. M. Potter and G. R. Rossman, *Am. Mineral.*, 1979, **64**, 1199–1218.
47 C. L. Lopano, P. J. Heaney, J. E. Post, J. Hanson and S. Komarneni, *Am. Mineral.*, 2007, **92**, 380–387.
48 J. E. Post and D. R. Veblen, *Am. Mineral.*, 1990, **75**, 477–489.